Shock Waves (2023) 33:533–551
https://doi.org/10.1007/s00193-023-01153-2

ORIGINAL ARTICLE

Extension of the normal shock wave relations for calorically imperfect gases

C. H. B. Civrais[1] · C. White[1] · R. Steijl[1]

Received: 31 March 2023 / Revised: 28 November 2023 / Accepted: 29 November 2023 / Published online: 28 February 2024

Abstract
An extension to the normal shock relations for a thermally perfect, calorically imperfect gas, modelling the vibrational excitation with an anharmonic oscillator model and including the influence of electronic modes, is derived and studied. Such additional considerations constitute an extension to the work achieved in the past, which modelled the caloric imperfections with a harmonic oscillator for vibrational energy and did not consider the effect of electronic energy. Additionally, the newly derived expressions provide physical insights into the limitations of experimentation for replicating flight conditions, which is demonstrated through providing solutions at different upstream temperatures. The results are compared with direct simulation Monte Carlo simulations for nitrogen and air, with the extent of the caloric imperfection of the gas showing excellent agreement. For low upstream temperatures, the extended relations are found to be in good agreement with the original normal shock wave expressions, but the results diverge for higher upstream temperatures that would be more representative of real flows. The results show that the new expressions depart from ideal gas theory for Mach numbers in excess of 4.9 at wind-tunnel conditions and for any Mach number above 3.0 at flight conditions. It is also shown that the traditional harmonic oscillator model and the anharmonic oscillator model begin to diverge at Mach number 3.0 for molecular oxygen gas and at Mach number 5.0 for an air mixture at flight conditions.

Keywords Normal shock waves · Caloric imperfection · Anharmonic oscillator · DSMC

1 Introduction

A normal shock wave is an idealised representation of common high-speed flow phenomena. For a vehicle flying at hypersonic flow conditions, a normal shock wave may be generated along the stagnation streamline. In inlet forebodies and deflected control surfaces of the vehicles, the flow experiences a more complex system of shock wave and boundary layer interactions [1–3] that are inherently different from a normal shock wave. Nevertheless, due to the absence of boundary effects and its inherent one-dimensionality, the normal shock wave is an appropriate problem to verify new models for capturing non-equilibrium and caloric imperfection effects. It allows one to estimate the benefits of various models, as well as to quantify the limitations of their applicability. The shock structure and property ratios have been extensively studied: theoretically [4–9], experimentally [10, 11], and numerically [12, 13] in the past. These articles only represent a selection of many more works available in the literature.

Both continuum and kinetic approaches are employed to resolve these structures with the use of the Navier–Stokes–Fourier equations [14] or moment methods [15] for the former, and the deterministic discrete velocity method [16] or the statistical direct simulation Monte Carlo (DSMC) [13] approach for the latter. The DSMC technique is a particle-based method which statistically approximates solutions to the Boltzmann equation. Each DSMC simulator particle represents a large number of real molecules/atoms and is moved ballistically, while collision events are treated stochastically after the movement step. Bird [12] has demonstrated that this method can successfully recover the normal shock

Communicated by S. O'Byrne.

✉ C. H. B. Civrais
clement.civrais@glasgow.ac.uk

C. White
craig.white.2@glasgow.ac.uk

R. Steijl
rene.steijl@glasgow.ac.uk

[1] James Watt School of Engineering, University of Glasgow, Glasgow G12 8QQ, UK

wave structures measured by Alsmeyer [17] for Mach numbers ranging from 1 to 9 of monoatomic species, i.e., Ar, and diatomic species, i.e., N_2. Additionally, Bird [13] has reported that normal shocks become rarefied for any Mach number of above 1.6 and therefore the Navier–Stokes solutions produce significant errors in the shock profiles; however, the pre- to post-shock property ratios remain well predicted for all Knudsen numbers using either continuum or rarefied methods, which was also predicted by Bethe and Teller [7]. Similar outcomes are also reported by Greenshields and Reese [18] for the study of Brenner's modified Navier–Stokes equations in shock structure problems. The DSMC approach is herein considered to simulate the flow properties across a normal shock wave for gases experiencing caloric imperfection, and the results are compared to an extended form of the Rankine–Hugoniot jump relations [4, 5] that will be derived in the current work.

In the computational fluids dynamics (CFD) community, real gas effects appear to be well understood, with the development of tools, such as Cantera [19], for various problems involving chemical kinetics, thermodynamics, and transport processes. NASA also provide standard tables of thermodynamic properties [20] that have been implemented in the Chemical Equilibrium with Applications (CEA) software [21, 22]. The caloric imperfection is frequently modelled with an empirical representation of the specific heat capacities involving polynomial expressions with five terms [23], later extended to eight terms [24]. However, some works assume the specific heat capacities to be constant [25] with respect to temperature. Others employ a more sophisticated approach in which the internal modes are treated individually [26]; although, the electronic mode is often omitted and the vibrational mode modelled with a harmonic oscillator model [26]. However, in the DSMC community, these real gas effects are perhaps not as well understood or handled; the models used often do not correctly capture the real gas effects [27]. New approaches are developed in the current article to accurately predict the properties of a gas that exhibits caloric imperfections, with care being taken to ensure that the DSMC and the Rankine–Hugoniot jump relations employ the same assumptions and models so that they can be compared fairly.

In theoretical studies of flows through normal shocks, the harmonic oscillator (HO) model for vibrational energy is often used and the electronic modes of the molecule are neglected [6, 8, 9, 28]. In the majority of the applications of DSMC to high-speed flows, a similar level of physical modelling based on the HO model and the exclusion of electronic modes [27, 29–32] is used. It is clear that the benefits of including the electronic mode increase with the temperature [33]. The omission of the electronic modes impacts the physical properties of the chemical species, resulting in the specific heat capacities being significantly underestimated at high temperatures, as has been shown for the oxygen molecule [33].

The HO model benefits from a simple form, having a linear dependence of vibrational energy to vibrational quantum levels, which, in turn, results in a straightforward derivation of the thermophysical flow properties. In the past, the HO model has been used to describe the vibrational excitation of a diatomic molecule for the calculation of downstream flow properties of a calorically imperfect gas behind a normal shock wave [32, 34, 35]. The result is a strong departure of the temperature ratio from the solution for an ideal air mixture as the Mach number increases. Similar behaviour has also been reported by Eggers [6]; however, this manuscript limited the investigation to translational, rotational, and vibrational modes only, where the vibrational excitation is modelled with the HO model. This model is a reasonable option for relatively low temperatures; however, it can lose its validity as the temperature increases. As a result of the linear distribution of the vibrational energy, the modelling of the thermodynamic properties, e.g., isochoric specific heat capacity, is inaccurate at high temperatures [33].

A more suitable approach is to consider the vibrational energy with an anharmonic oscillator (aHO) model. An aHO model is usually structured with a harmonic term upfront and a succession of nonlinear anharmonic terms. A wide range of aHO models are available in the literature [36]; in the present work, the Morse-aHO model [37] is considered. It has proven to return excellent results in the recovery of thermodynamic flow properties for diatomic gases [24, 38]. This change from HO to aHO model allows for more accurate modelling of the physics of the flow. Having an aHO model to compute the downstream flow properties behind a normal shock wave would constitute a significant improvement on the studies conducted by Eggers [6] and Blackman [9].

From statistical thermodynamics theory [28, 39], it is clear that the consideration of the full set of internal modes is indispensable for the correct modelling of the thermodynamic properties of the molecular system. Although this is a fundamental principle in the study of particle dynamics-related phenomena, to the authors' knowledge, most of the aforementioned works do not quantify the importance of each of the modes, in particular the electronic mode, on the physical properties of a molecular system.

The current work proposes an extension of the work achieved by Eggers [6], by NASA [8], and by Blackman [9], including an aHO model for the vibrational energies and the electronic states of the molecular system in the normal shock relations. A key contribution of this work is the mathematical derivation of the normal shock relations for a calorically imperfect gas in which the vibrational mode is handled with an aHO model and the electronic mode is included, which to the best of the authors' knowledge has not previously been derived or studied. These new relations are applied to quan-

tifying the influence of vibrational models and electronic excited states on post-shock equilibrium conditions. Additionally, it aims to provide physical insight into the limitations of experiments for replicating real conditions where a strong normal shock may be found, by evaluating the impact of these improved models on the post-shock equilibrium conditions as a function of upstream static temperature. The evaluation of downstream flow properties with an aHO model consists of resolving a nonlinear system by employing an iterative approach; the derivation and computation of downstream flow properties will be detailed in Sect. 2.

The rest of the paper is organised as follows. Section 2 demonstrates the new mathematical model for the downstream flow properties in a normal shock wave for a calorically imperfect gas. In Sect. 3, the numerical methods and problem configurations employed for the simulation of a normal shock wave with *dsmcFoam+* are developed. Section 4 investigates the influence of the vibrational model and the inclusion of the electronic mode on the flow properties downstream of a normal shock wave for a pure gas and a gas mixture. The last section provides conclusions and perspectives for future work.

2 Mathematical description

2.1 Shock wave relations

For a one-dimensional, adiabatic, inviscid, non-reacting, compressible flow, the governing equations are the Rankine–Hugoniot jump relations [4, 5], which relate the upstream and downstream flow properties,

$$\begin{cases} \rho_1 u_1 = \rho_2 u_2 \\ P_1 + \rho_1 u_1^2 = P_2 + \rho_2 u_2^2 \\ \hat{h}_1 + \frac{u_1^2}{2} = \hat{h}_2 + \frac{u_2^2}{2}, \end{cases} \tag{1}$$

where u is flow velocity, ρ is density, P is pressure, $\hat{h}$ is enthalpy, and the subscripts $(\cdot)_1$ and $(\cdot)_2$ refer to the upstream and downstream flow properties, respectively.

For typical conditions encountered in ground test facilities and in high-speed flight, the departure from the ideal gas assumption is negligible for light gases [6, 40]. Therefore, in this study the gas, i.e., mixtures of O_2 and N_2, are regarded as thermally perfect, calorically imperfect, with the result that the gas obeys the ideal gas law and the caloric equation of state [28]. With the three jump relations, (1), and the two equations of state, the system is fully defined, having five equations for five downstream flow properties. In a situation where the gas relies on ideal theory, the downstream flow properties can all be expressed as a function of the upstream Mach number. In this work, a more realistic approach has been chosen to recover the physics of the flow with the use of a calorically imperfect equation of state.

Since the gas is considered thermally perfect, the caloric equation of state can be reformulated as,

$$\mathrm{d}\hat{h} = (C_v(T) + R)\mathrm{d}T, \tag{2}$$

where C_v is the specific heat capacity at constant volume, R is the specific gas constant, and T is the temperature.

The next step is to expand the expression of $C_v(T)$ to outline the contribution of each mode as,

$$\frac{C_v(T)}{R} = \frac{5}{2} + \frac{1}{k}\left(\frac{\partial E_\mathrm{v}(T)}{\partial T} + \frac{\partial E_\mathrm{e}(T)}{\partial T}\right), \tag{3}$$

where k is the Boltzmann constant, $E(T)$ is the total mean energy of each molecule, and the subscripts $(\cdot)_\mathrm{v}$ and $(\cdot)_\mathrm{e}$ refer, respectively, to the vibrational and electronic contribution.

The general expression of the total mean energy $E(T)$ is formulated as,

$$E(T) \equiv \frac{\sum_i g_i \epsilon(i) \mathrm{e}^{\frac{-\epsilon(i)}{kT}}}{\sum_i g_i \mathrm{e}^{\frac{-\epsilon(i)}{kT}}}, \tag{4}$$

where g_i is the degeneracy of the ith state and ϵ is the internal energy associated with the quantum level i.

At this stage, Eggers [6], NASA [8], and Blackman [9] compute the vibrational energies with the HO model defined as,

$$\epsilon_\mathrm{v}^\mathrm{HO}(i) = ik\theta_\mathrm{v}, \tag{5}$$

where ϵ_v is the vibrational energy, i is the vibrational quantum level, and θ_v is the characteristic vibrational temperature of a chosen gas.

In the current work, an improvement upon this is proposed: modelling the vibrational excitation with the Morse-aHO model [37] in which the vibrational energies are formulated as,

$$\epsilon_\mathrm{v}^\mathrm{Morse}(i) = hc\omega_\mathrm{e} i(1 - \chi_\mathrm{e}(i+1)), \tag{6}$$

where h is the Planck constant, c is the speed of light in vacuum, and ω_e and $\omega_\mathrm{e}\chi_\mathrm{e}$ are spectroscopy constants detailed in Table 2 for nitrogen and oxygen molecules.

Substituting (4) into (3), inserting the result into (2), and applying definite integrals, the enthalpy of the flow accounting for vibrational and electronic modes yields,

$$\hat{h}(T) = \frac{5}{2}RT + \frac{\sum_i \epsilon_\mathrm{v}(i)\mathrm{e}^{\frac{-\epsilon_\mathrm{v}(i)}{kT}}}{\sum_i \mathrm{e}^{\frac{-\epsilon_\mathrm{v}(i)}{kT}}} + \frac{\sum_i g_i \epsilon_\mathrm{e}(i)\mathrm{e}^{\frac{-\epsilon_\mathrm{e}(i)}{kT}}}{\sum_i g_i \mathrm{e}^{\frac{-\epsilon_\mathrm{e}(i)}{kT}}}. \tag{7}$$

The electronic energy of the molecular systems are those prescribed by Liechty [41], which have been extracted from the National Institute of Standards and Technology (NIST) [42].

With the added complication of a calorically imperfect gas, the enthalpy is no longer linearly related to the temperature and the system must be resolved iteratively. Several methodologies could be applied, such as the Newton iterative method [33], a dichotomy approach, or any other type of root-finding algorithm [21]. In the current work, the chosen approach follows the technique presented by Anderson [43]. It consists of maintaining the energy balance across the shock wave through the following equation,

$$(\hat{h}_2 - \hat{h}_1) + \frac{u_1^2}{2}\left(\frac{1}{\rho_{21}^2} - 1\right) = 0. \tag{8}$$

The iterative approach is initialised with a guessed value for the density ratio, $\rho_{21,\text{ini}}$. Although a departure from the ideal gas theory is expected, the ideal gas formulation for the density ratio can be used to initialise the iterative calculation,

$$\rho_{21}^* = \frac{(\gamma+1)M_1^2}{2+(\gamma-1)M_1^2}, \tag{9}$$

where M is the Mach number, the subscript $(\cdot)_{21}$ characterises the ratio between the downstream and upstream flow properties, the superscript $(\cdot)^*$ refers to flow properties of an ideal gas, and γ is the ratio of specific heats, defined as

$$\gamma = \frac{C_p}{C_v}. \tag{10}$$

Once the density ratio is obtained, the pressure ratio can be found by re-arranging the momentum equation and the temperature ratio by applying the thermal equation of state, i.e.,

$$\begin{cases} P_{21} = 1 + \frac{\rho_1 u_1^2}{P_1}\left(1 - \frac{1}{\rho_{21}}\right), \\ T_{21} = \frac{P_{21}}{\rho_{21}}. \end{cases} \tag{11}$$

Finally, the density ratio is either increased or decreased, depending on the sign of the energy balance, (8), by an increment $\Delta\rho_{21}$, and the procedure is repeated until convergence is achieved, where $\Delta\rho_{21}$ takes the form of,

$$\Delta\rho_{21} = \begin{cases} \frac{1}{10} & \text{if } j = 0, \\ \frac{1}{10j\sqrt{j}} & \text{if } j \neq 0, \end{cases} \tag{12}$$

where j refers to the iteration index.

2.2 Stability analysis

Balancing the energy equation, (8), is a sensitive problem; therefore, the initialised density, (9), and the increment value of density, (12), must be carefully chosen. A sensitivity analysis of the new relations to these parameters is conducted.

The working gas is molecular oxygen where the vibrational energies are modelled with an anharmonic oscillator model and the electronic energies included. The freestream conditions correspond to an altitude of 80 km [44], i.e., $P = 1.1$ Pa and $T = 198.6$ K, which results in a freestream enthalpy of 1.29×10^5 J/kg. The analysis is carried out for three Mach numbers, i.e., 2, 5, and 8. The initialised value and increment value of density are perturbed compared to those prescribed by (9) and (12), respectively. These perturbed parameters are denoted by $\tilde{\rho}_{21}^*$ and $\Delta\tilde{\rho}_{21}$ for the initialised density and the increment value of density, respectively. The system is exposed to perturbations ranging from $\pm 50\%$ of the suggested values, i.e., (9) and (12), with increments of 10%. The simulations are run for a total number of 1000 iterations. The energy balance achieved through these iterations and the flow property ratios are monitored for each pair of $(\tilde{\rho}_{21}^*, \Delta\tilde{\rho}_{21})$.

The influence of these parameters on the energy balance for three Mach numbers is depicted in Fig. 1. The abscissa represents the perturbations in the increment value of density, the ordinate corresponds to the perturbations of the initialised density, while the colour map shows the energy balance achieved through the iterations. Note that the colour scheme is expressed in logarithmic scale. The black markers correspond to conditions at which the influence of the quality of the energy balance on the flow properties will later be discussed. Considering the sensitivity of the system, any set of parameters achieving an energy balance of 10^1 J/kg and below is considered acceptable. Note that the freestream enthalpy is 1.29×10^5 J/kg which translates to a deviation of 0.01% to the freestream enthalpy.

For Mach number 2, the system achieves satisfactory energy conservation for most of the conditions except for initialised density values lower than $0.6\rho_{21}^*$. For such freestream conditions, the flow properties are expected to exhibit no caloric imperfection; therefore, initialising the system close to its final solution achieves the best convergence. For initialised guess values lower than $0.6\rho_{21}^*$ and increment density values, $\frac{\Delta\tilde{\rho}_{21}}{\Delta\rho_{21}} \in [0.5, 0.6\,[\cup]\,1.4, 1.5]$ the system achieves poor energy conservation. It is important to note that a total number of 1000 iterations is considered in the current study. Therefore, it would necessitate additional iterations to achieve satisfactory energy balancing. For higher Mach numbers, the system deviates from the ideal gas theory, resulting in an increase in the density ratio. Consequently, the system benefits from being initialised at higher density ratios. Such

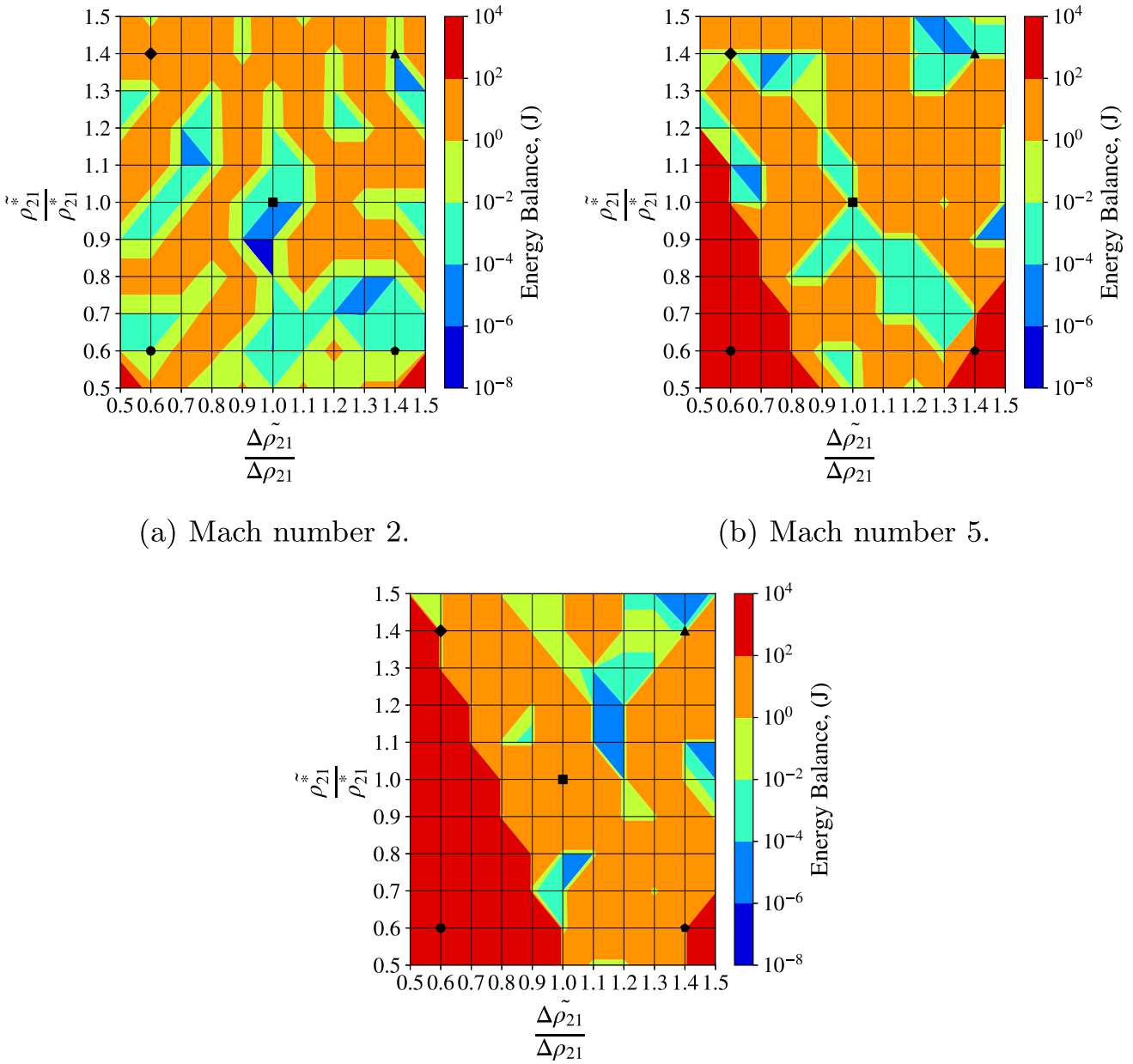

(a) Mach number 2.

(b) Mach number 5.

(c) Mach number 8.

Fig. 1 Influence of the initialised density value and increment value of density on the energy conservation for three Mach numbers

a behaviour is demonstrated in Fig. 1 in which the area of acceptable energy balances is reduced with increased Mach number.

The influence of these parameters on the density, pressure, and temperatures ratios is investigated for the five conditions indicated by the black markers in Fig. 1. These conditions have been carefully chosen to evaluate the consequences of poor energy balancing. The results are depicted in Fig. 2, and the flow properties ratio for a calorically perfect gas is added for reference. The circle (○), square (□), triangle (△), diamond (◇), and pentagon (⬠) markers refer to those in Fig. 1.

Figure 2 reiterates the importance of carefully selecting the initial density value and the increment value of density. The sets of parameters predict similar flow properties for low Mach numbers but strongly deviate with an increase in Mach number. It is also important to mention that the triangle, square, diamond, and pentagon markers are on top of each other even though the sets of parameters achieve different energy balances, see Fig. 1, which demonstrates that for an

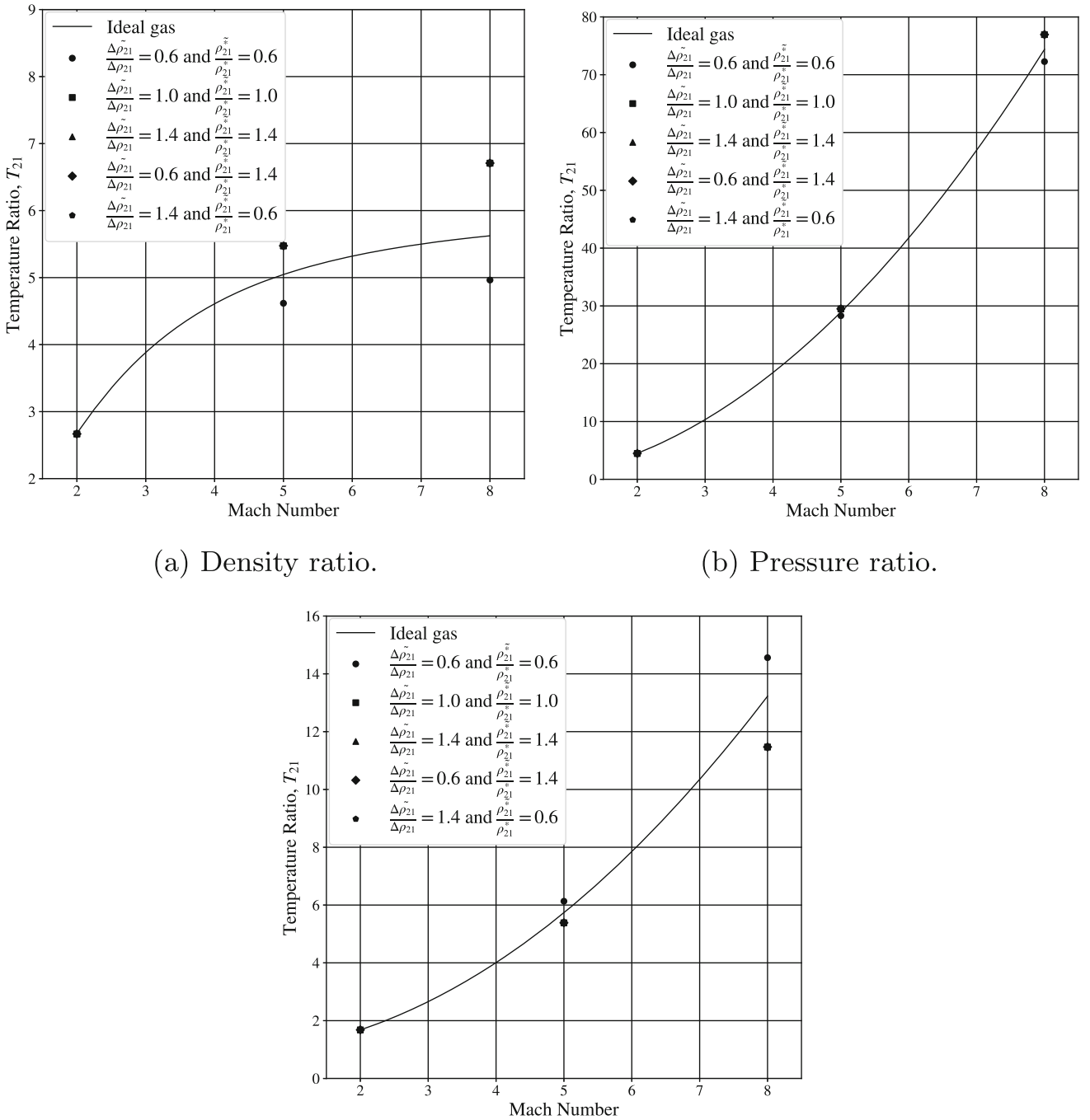

Fig. 2 Influence of the initialised density value and increment value of density on the flow properties

energy balance below 10^1 J/kg the flow properties converge towards similar predictions.

Figures 1 and 2 have shown that the initial density value and increment density value suggested in the previous sections, i.e., $\frac{\tilde{\rho_{21}}}{\rho^{*}_{21}} = 1.0$ and $\frac{\Delta\tilde{\rho}_{21}}{\Delta\rho_{21}} = 1.0$, achieve satisfactory energy balance for the freestream conditions considered. This set of parameters will therefore be used for the calculation of the flow properties ratios across the shock. As noticed, for high Mach numbers in which the flow likely exhibits caloric imperfection, the system could benefit from being initialised at a higher initial density ratio. Ideally, these sets of parameters would be a function of the freestream con-

ditions, i.e., Mach number and enthalpy; however, such an improvement would merely decrease how many iterations are required to converge the system. For the other calculations presented in the current work, a maximum of 150 iterations were required to achieve energy balancing below 10^{-3} J/kg. Improving the convergence speed of the system was therefore considered irrelevant.

2.3 Model limitations

The model presented in this study yields accurate predictions, see Sects. 4.2 and 4.3, but it does have limitations which merit additional discussion.

In the derivation of the model, the Born–Oppenheimer approximation is assumed which allows for the internal modes to be individually treated. As such, the total mean energy of the system is expressed as the summation of independent contributions, as shown in (3)–(7). This assumption is valid for the temperatures dealt with in the current work. However, for higher temperatures, the model would benefit from modelling the internal interaction between modes. Specifically, accounting for the vibrational excitation of the electronic excited states becomes important for moderate-to-high temperatures, while rotational-vibrational effects become significant at high temperatures. To improve the accuracy of the model, incorporating these effects in the calculation of the thermodynamic properties would be necessary.

Furthermore, the model assumes that any chemical activity is slow enough for the chemical reactions to be omitted. This assumption follows that of Eggers [6] and Blackman [9] for the derivation of normal shock wave relations for calorically imperfect gases. This limitation constrains the new relations to be strictly employed in flow regimes where the effects of chemical reactions are insignificant. As reported by Eggers [6], this corresponds to Mach numbers in excess of 7 for an air mixture at sea-level atmospheric conditions [44], which translates to an enthalpy of the system downstream of the shock wave of 2.2×10^6 J/kg. This particular threshold aligns with observations made by Leyva [45], who similarly defines the maximum stagnation enthalpy for an air mixture at 5.0×10^6 J/kg. For higher enthalpies, chemical species carry enough energy for chemical reactions to occur and strongly affect the downstream flow properties [46]. The addition of chemical reactions to the model in the form of a partition function is proposed as a next step, given the derivations detailed in Fowler and Guggenheim [47]. This improvement would have the benefit of further extending the range of applicability of the model to higher Mach numbers and enthalpies. In the rest of the paper, the validity of the model will be restricted to the enthalpy value prescribed by Eggers.

Table 1 Case scenarios studied in the present work

Scenario	T_1 (K)	P_1 (Pa)	Species
I	48.4	227.0	O_2, air
II	100.0	55.3	O_2, air
III	198.6	1.1	O_2, air

3 Numerical methods and problem setup

3.1 Simulation outline

This work consists of verifying the aforementioned mathematical relations, see Sect. 2, with shock wave simulations using a single species diatomic gas and a gas mixture. Three freestream conditions are considered based on wind-tunnel operating conditions for the 20-inch Mach 6 tunnel and hypersonic nitrogen tunnel in Beckwith and Miller [48, Table 1], and a more realistic flight condition at an altitude of 80 km [44]. The freestream pressures and temperatures for each scenario are tabulated in Table 1. The choice has been made to use similar freestream conditions for the two working gases. To prevent the occurrence of chemical reactions, the maximum Mach numbers allowed for the downstream enthalpy of the system to lie below the threshold defined by Eggers [6] has been computed for each scenario. For the freestream conditions in scenarios I, II, and III, the maximum Mach numbers are, respectively, 18.5, 12.5, and 9.0 for an oxygen gas and 17.5, 12.0, and 8.5 for an air mixture (79% N_2 and 21% O_2). It is worth noticing that for scenarios I, II, and III, the model exhibits different maximum Mach numbers depending on the gas considered. This can be attributed to distinct thermal variations in the specific heat capacities of the gases in consideration, see Sect. 4.1. These Mach numbers represent the theoretical limitations of the model presented in the study for scenarios I, II, and III. It is important to note that these conditions are not typically encountered in wind-tunnels. In light of these findings, the study exclusively focuses on Mach numbers ranging from 2 to 8 for all three scenarios. Additionally, three DSMC simulations at Mach numbers of 2, 5, and 8 are run to verify the Rankine–Hugoniot jump relations and the implementation of the models in the DSMC code.

3.2 Numerical methods

All the simulations presented in this work have been conducted using the *dsmcFoam+* [49] solver, which is a DSMC solver developed around the foundation of the method established by Bird [13]. It is built within the framework of the open-source C++ computational fluid dynamics toolbox OpenFOAM [50]. The main features of the *dsmcFoam+* code

Table 2 Species properties at a reference temperature T_{ref} of 273 K

Chemical species	m ($\times 10^{-27}$ kg)	d ($\times 10^{-10}$ m)	ω (–)	θ_v (K)	ω_e [33] (cm^{-1})	$\omega_e \chi_e$ [33] (cm^{-1})
N_2	46.50	4.17	0.74	3371	2345.998	17.454
O_2	53.12	4.07	0.77	2256	1671.740	16.425

include particle initialisation in arbitrary geometries, particle tracking in unstructured meshes, the capability to perform both steady-state and transient DSMC simulations, chemical reactions, vibrational and electronic energies, and parallel processing [49]. In the current work, a version of *dsmcFoam+* that is implemented within OpenFOAM-v2212 is used. To provide a more realistic description of the vibrational excitation of a diatomic molecule, an aHO model derived from the Morse potential [37] has been implemented in *dsmcFoam+*. As extensively described in Civrais et al. [33, 51], rather than computing the vibrational energy through the use of the characteristic vibrational temperature, aHO vibrational levels have been pre-calculated and inserted within the *dsmcFoam+* species definitions as an additional "look-up table" entry. The vibrational energy of the molecular species is modelled with the Morse anharmonic oscillator model with a set of 67 and 47 vibrational quantum levels for N_2 and O_2, respectively, as prescribed by the potential energy surface (PES) calculations detailed in Armenise et al. [52]. It has been shown that having an aHO model representing the vibrational excitation of diatomic molecules results in an improved prediction of the specific heat capacity. This remark will be reinforced by the evaluation of the influence of the use of an aHO model in the context of high-speed non-equilibrium situations.

The redistribution of internal energies is ensured by a serial application of the quantum Larsen–Borgnakke (LB) method [53] using the HO model or the Morse-aHO model [33] to compute the vibrational energy of the molecule. A finite fraction of 1/5, 1/50, and 1/500 collisions is allowed to result in rotational, vibrational, and electronic relaxation, respectively. The inter-molecular collisions are modelled using the variable hard sphere (VHS) model at a reference temperature of $T_{ref} = 273$ K with the species properties summarised in Table 2, and the collision partners are selected according to the no-time-counter (NTC) model [54]. This work aims to quantify the influence of vibrational models and electronic energy on equilibrium states reached downstream of a normal shock wave, as these ratios are all that the Rankine–Hugoniot method can predict; the transitional region, in which internal modes relax towards the equilibrium state, is not intended to be quantitatively studied in this work.

3.3 Problem setup

The DSMC simulations are set up as follows. All normal shock simulations are initialised with a uniform spatial domain discretised in the direction of the discontinuity with the driving piston boundary condition applied [13]. The cell size throughout the domain is set to be equal to one-quarter of the high pressure, i.e., post-shock, mean free path [55]. The longitudinal length of the domain, L, is set to 331.8×10^{-3} m, 442.4×10^{-3} m, and 553.0×10^{-3} m for the Mach number 2, 5, and 8 cases, respectively. The number of cells and particles are therefore adapted to match the spatial discretisation with a minimum of 20 particles per cell in the low-density region. For each case, the time-step is carefully chosen to be an order of magnitude smaller than both the mean collision time and the cell residence time, with the former corresponding to the time a typical DSMC particle requires to cross a cell length in the upstream conditions. The simulations are performed in serial on a machine equipped with an Intel® Core™ i7-7820X x16 CPU (3.62 GHz). Flow properties are sampled for over 10^5 time-steps and averaged over 1000 cells on both sides of the discontinuity to reduce the scatter.

The domain is spatially split into two equally sized regions where the appropriate upstream and downstream conditions, see Sect. 2, are initially prescribed, creating a discontinuity at the centre. This technique is known to return a good approximation of experimental conditions [56] but induces a translation of the shock front due to random walks [13]. Therefore, a stabilisation routine has been implemented within *dsmcFoam+* to prevent the shock from moving in one direction or the other.

4 Results and discussion

4.1 Thermodynamic properties

4.1.1 Oxygen

A comparison of the normalised isochoric specific heat capacity, i.e., C_v/R, resulting from the different internal energy models is presented for molecular oxygen in Table 3 for temperatures ranging from 200 to 7000 K. The database

Table 3 Comparison of the different approaches for the calculation of the normalised isochoric specific heat capacity of molecular oxygen

T (K)	Ideal	HO	aHO	HOe	aHOe	McBride et al. [24]
200	2.500 (0.1%)	2.501 (0.1%)	2.501 (0.1%)	2.501 (0.1%)	2.501 (0.1%)	2.503
400	2.500 (4.7%)	2.590 (1.2%)	2.597 (0.9%)	2.590 (1.2%)	2.597 (0.9%)	2.622
600	2.500 (12.6%)	2.804 (1.9%)	2.819 (1.4%)	2.804 (1.9%)	2.819 (1.4%)	2.860
800	2.500 (18.3%)	2.996 (2.0%)	3.014 (1.4%)	2.996 (2.0%)	3.014 (1.4%)	3.059
1000	2.500 (21.8%)	3.132 (2.0%)	3.153 (1.3%)	3.133 (2.0%)	3.154 (1.3%)	3.195
1200	2.500 (24.1%)	3.224 (2.1%)	3.248 (1.4%)	3.229 (2.0%)	3.252 (1.2%)	3.293
1400	2.500 (25.7%)	3.287 (2.3%)	3.314 (1.5%)	3.300 (1.9%)	3.327 (1.1%)	3.364
1600	2.500 (27.0%)	3.332 (2.8%)	3.362 (1.9%)	3.359 (2.0%)	3.390 (1.1%)	3.427
1800	2.500 (28.3%)	3.364 (3.5%)	3.398 (2.5%)	3.412 (2.1%)	3.447 (1.1%)	3.486
2000	2.500 (29.5%)	3.388 (4.4%)	3.426 (3.3%)	3.463 (2.3%)	3.501 (1.2%)	3.544
2200	2.500 (30.6%)	3.406 (5.4%)	3.449 (4.2%)	3.511 (2.5%)	3.553 (1.3%)	3.601
2400	2.500 (31.6%)	3.421 (6.4%)	3.468 (5.1%)	3.557 (2.7%)	3.604 (1.4%)	3.656
2600	2.500 (32.6%)	3.432 (7.5%)	3.484 (6.1%)	3.601 (2.9%)	3.652 (1.5%)	3.709
2800	2.500 (33.5%)	3.441 (8.5%)	3.497 (7.0%)	3.642 (3.1%)	3.699 (1.6%)	3.760
3000	2.500 (34.4%)	3.448 (9.5%)	3.510 (7.8%)	3.680 (3.4%)	3.742 (1.7%)	3.808
3200	2.500 (35.1%)	3.454 (10.4%)	3.521 (8.6%)	3.715 (3.6%)	3.782 (1.9%)	3.855
3400	2.500 (35.9%)	3.459 (11.3%)	3.532 (9.4%)	3.747 (3.9%)	3.819 (2.0%)	3.899
3600	2.500 (36.5%)	3.464 (12.1%)	3.542 (10.1%)	3.775 (4.2%)	3.853 (2.2%)	3.940
3800	2.500 (37.2%)	3.467 (12.9%)	3.552 (10.7%)	3.800 (4.5%)	3.884 (2.4%)	3.979
4000	2.500 (37.8%)	3.471 (13.6%)	3.562 (11.3%)	3.822 (4.8%)	3.913 (2.6%)	4.016
4200	2.500 (38.3%)	3.473 (14.3%)	3.571 (11.8%)	3.841 (5.2%)	3.939 (2.8%)	4.051
4400	2.500 (38.8%)	3.476 (14.9%)	3.581 (12.3%)	3.857 (5.6%)	3.962 (3.0%)	4.084
4600	2.500 (39.2%)	3.478 (15.5%)	3.590 (12.7%)	3.871 (5.9%)	3.984 (3.2%)	4.115
4800	2.500 (39.7%)	3.479 (16.0%)	3.600 (13.1%)	3.884 (6.3%)	4.005 (3.4%)	4.144
5000	2.500 (40.1%)	3.481 (16.5%)	3.610 (13.5%)	3.895 (6.6%)	4.024 (3.5%)	4.171
5200	2.500 (40.4%)	3.482 (17.0%)	3.620 (13.7%)	3.905 (7.0%)	4.043 (3.7%)	4.197
5400	2.500 (40.8%)	3.484 (17.5%)	3.631 (14.0%)	3.915 (7.3%)	4.062 (3.8%)	4.222
5600	2.500 (41.1%)	3.485 (17.9%)	3.641 (14.2%)	3.923 (7.6%)	4.080 (3.9%)	4.244
5800	2.500 (41.4%)	3.486 (18.3%)	3.652 (14.4%)	3.932 (7.8%)	4.098 (3.9%)	4.266
6000	2.500 (41.7%)	3.487 (18.6%)	3.662 (14.6%)	3.940 (8.1%)	4.116 (4.0%)	4.286
6200	2.500 (41.8%)	3.488 (18.9%)	3.672 (14.6%)	3.949 (8.1%)	4.134 (3.8%)	4.299
6400	2.500 (42.0%)	3.488 (19.1%)	3.683 (14.6%)	3.958 (8.2%)	4.152 (3.7%)	4.311
6600	2.500 (42.2%)	3.489 (19.3%)	3.693 (14.5%)	3.967 (8.2%)	4.171 (3.5%)	4.322
6800	2.500 (42.2%)	3.490 (19.4%)	3.703 (14.5%)	3.977 (8.1%)	4.190 (3.2%)	4.329
7000	2.500 (42.3%)	3.490 (19.4%)	3.712 (14.3%)	3.987 (8.0%)	4.209 (2.8%)	4.333

HOe and aHOe denote the inclusion of the electronic mode

presented by McBride et al. [24] is well established and is therefore considered as reference data. This database includes the electronic, rotational, and harmonic oscillator vibrational contributions to the partition function, and accounts for various corrections, including anharmonicity, the vibrational excitation of the electronic excited states, and the rotational-vibrational effects [57, p. 11]. The deviation of each internal energy model considered in the current work with respect to the values in McBride et al. [24] is expressed in percentages. For completeness, the results for the ideal gas assumption are also included in Table 4 and denoted by Ideal in the table.

In the DSMC community, the vibrational excitation is frequently modelled with the HO model and the electronic mode is neglected, resulting in a deviation of the isochoric specific heat capacity of approximately 19.4% compared to the McBride et al. [24] database at a temperature of 7000 K. Even at lower temperatures where dissociation would not be considered, the deviation in the HO model from the reference data is significant. Considering the harmonic oscillator model with electronic mode included (HOe), decreases the

Table 4 Comparison of the different approaches for the calculation of the normalised isochoric specific heat capacity of an air mixture composed of 79% nitrogen and 21% oxygen

T (K)	Ideal	HO	aHO	HOe	aHOe	McBride et al. [24]
200	2.500 (0.1%)	2.500 (0.0%)	2.500 (0.0%)	2.500 (0.0%)	2.500 (0.0%)	2.501
400	2.500 (1.6%)	2.531 (0.3%)	2.534 (0.2%)	2.531 (0.3%)	2.534 (0.2%)	2.540
600	2.500 (6.4%)	2.655 (0.6%)	2.664 (0.3%)	2.655 (0.6%)	2.664 (0.3%)	2.671
800	2.500 (11.9%)	2.818 (0.7%)	2.830 (0.3%)	2.818 (0.7%)	2.830 (0.3%)	2.839
1000	2.500 (16.3%)	2.964 (0.8%)	2.978 (0.3%)	2.964 (0.8%)	2.978 (0.3%)	2.988
1200	2.500 (19.5%)	3.078 (0.9%)	3.094 (0.4%)	3.079 (0.9%)	3.095 (0.4%)	3.106
1400	2.500 (21.8%)	3.163 (1.0%)	3.181 (0.5%)	3.166 (0.9%)	3.184 (0.4%)	3.196
1600	2.500 (23.5%)	3.228 (1.2%)	3.247 (0.6%)	3.234 (1.0%)	3.253 (0.4%)	3.267
1800	2.500 (24.8%)	3.276 (1.5%)	3.298 (0.8%)	3.286 (1.1%)	3.308 (0.5%)	3.325
2000	2.500 (25.9%)	3.314 (1.7%)	3.338 (1.0%)	3.329 (1.3%)	3.353 (0.6%)	3.372
2200	2.500 (26.7%)	3.343 (2.0%)	3.369 (1.3%)	3.364 (1.4%)	3.391 (0.6%)	3.412
2400	2.500 (27.5%)	3.365 (2.4%)	3.394 (1.5%)	3.394 (1.5%)	3.423 (0.7%)	3.447
2600	2.500 (28.1%)	3.384 (2.7%)	3.415 (1.8%)	3.419 (1.7%)	3.451 (0.8%)	3.477
2800	2.500 (28.6%)	3.399 (3.0%)	3.433 (2.0%)	3.441 (1.8%)	3.475 (0.8%)	3.504
3000	2.500 (29.1%)	3.411 (3.3%)	3.448 (2.3%)	3.460 (1.9%)	3.496 (0.9%)	3.528
3200	2.500 (29.6%)	3.421 (3.6%)	3.461 (2.5%)	3.476 (2.1%)	3.516 (1.0%)	3.550
3400	2.500 (30.0%)	3.430 (3.9%)	3.472 (2.7%)	3.490 (2.2%)	3.533 (1.0%)	3.570
3600	2.500 (30.3%)	3.437 (4.2%)	3.483 (2.9%)	3.503 (2.4%)	3.548 (1.1%)	3.588
3800	2.500 (30.7%)	3.443 (4.5%)	3.492 (3.1%)	3.513 (2.5%)	3.562 (1.2%)	3.605
4000	2.500 (31.0%)	3.449 (4.8%)	3.500 (3.3%)	3.522 (2.7%)	3.574 (1.3%)	3.621
4200	2.500 (31.2%)	3.453 (5.0%)	3.508 (3.5%)	3.531 (2.9%)	3.586 (1.4%)	3.636
4400	2.500 (31.5%)	3.457 (5.3%)	3.516 (3.7%)	3.538 (3.1%)	3.596 (1.5%)	3.650
4600	2.500 (31.8%)	3.461 (5.5%)	3.523 (3.8%)	3.544 (3.3%)	3.606 (1.6%)	3.664
4800	2.500 (32.0%)	3.464 (5.8%)	3.530 (4.0%)	3.549 (3.5%)	3.615 (1.7%)	3.677
5000	2.500 (32.3%)	3.467 (6.1%)	3.536 (4.2%)	3.554 (3.7%)	3.624 (1.8%)	3.690
5200	2.500 (32.5%)	3.469 (6.3%)	3.543 (4.3%)	3.559 (3.9%)	3.632 (1.9%)	3.703
5400	2.500 (32.7%)	3.471 (6.6%)	3.549 (4.5%)	3.563 (4.1%)	3.641 (2.0%)	3.716
5600	2.500 (33.0%)	3.473 (6.9%)	3.555 (4.7%)	3.567 (4.4%)	3.649 (2.2%)	3.730
5800	2.500 (33.2%)	3.475 (7.2%)	3.561 (4.9%)	3.571 (4.6%)	3.657 (2.3%)	3.744
6000	2.500 (33.5%)	3.477 (7.5%)	3.567 (5.1%)	3.575 (4.9%)	3.666 (2.5%)	3.759

HOe and aHOe denote the inclusion of the electronic mode

discrepancy in the isochoric specific heat capacity prediction to 8% at 7000 K. Considering an anharmonic oscillator model and, in particular, including the electronic mode, dramatically reduces the relative difference to 2.8% at 7000 K. It was expected that the anharmonic oscillator with electronic energy included (aHOe) model would best match the reference data since this model best matches the assumptions included in the calculation of the reference data. It is clear that the HO model starts to introduce significant errors at temperatures as low as 2000 K for molecular oxygen. Introducing the electronic energy always results in a significantly more accurate reproduction of the specific heat capacity, for either HO or aHO vibrations.

4.1.2 Air mixture

Table 4 repeats the comparison of the isochoric specific heat capacity calculated with the different approaches for an air mixture composed of 79% nitrogen and 21% oxygen for temperatures ranging from 200 to 6000 K. The temperature range is conditioned by the temperature intervals in which the coefficient of the polynomial expressions is valid. Similar to the previous comparison, HO displays the worst predictions, whereas the aHOe model presents close agreement with the reference database [24], with a deviation of 2.5% at a temperature of 6000 K.

4.2 Oxygen shock wave

The numerical investigation of nonreactive oxygen aims to evaluate the departure from ideality of downstream flow properties in a normal shock wave. The first step is to quantify how the four corrections, i.e., the HO or aHO models and the electronic mode included or not, change the post-shock equilibrium state and which flow properties are impacted. Then, the study seeks to demonstrate the departure from the ideal gas theory for pure oxygen gas.

The comparison of the normal shock wave relations with caloric imperfection and the DSMC results for the pressure, density, and temperature ratios is presented in Tables 5, 6, and 7, respectively. In Tables 5, 6, and 7, the vibrational models are denoted by their corresponding acronyms and the inclusion of the electronic mode by HOe or aHOe. For completeness, the percentage deviation of the numerical results to the Rankine–Hugoniot calculations has been added to Tables 5, 6, and 7. Furthermore, the standard normal shock wave relations [4, 5] without the consideration of caloric imperfection are included as a reference, and it is denoted by NC.

Table 5 presents a comparison of the pressure ratios between the normal shock wave relations with caloric imperfection and the DSMC results for the three upstream conditions. Agreement to three significant figures is observed between the Rankine–Hugoniot calculations and the DSMC results for all simulated upstream Mach number and temperature conditions. For a wind-tunnel operating at the scenario I conditions, the caloric imperfection has a minimal influence on the pressure ratio and it only departs from ideal gas theory for Mach number 6.8 and above. Note that the inclusion

Table 5 Comparison of the pressure ratio for a nonreactive pure oxygen gas

M	NC [4, 5]	Theory				DSMC			
		HO [6]	HOe	aHO	aHOe	HO	HOe	aHO	aHOe
Scenario I									
2	4.49	4.49	4.49	4.49	4.49	4.51 (0.4%)	4.51 (0.4%)	4.51 (0.4%)	4.51 (0.4%)
5	28.95	28.95	28.95	28.95	28.95	28.91 (−0.1%)	28.91 (−0.1%)	28.91 (−0.1%)	28.91 (−0.1%)
8	74.38	74.66	74.66	74.69	74.69	74.75 (0.1%)	74.85 (0.2%)	74.85 (0.2%)	74.6 (−0.1%)
Scenario II									
2	4.49	4.49	4.49	4.49	4.49	4.51 (0.4%)	4.51 (0.4%)	4.51 (0.4%)	4.51 (0.4%)
5	28.95	29.03	29.03	29.04	29.04	28.91 (−0.4%)	28.91 (−0.4%)	29.41 (1.3%)	28.94 (−0.4%)
8	74.38	75.78	75.79	75.83	75.83	76.25 (0.6%)	75.61 (−0.2%)	75.99 (0.2%)	76.35 (0.7%)
Scenario III									
2	4.49	4.49	4.49	4.49	4.49	4.50 (0.1%)	4.50 (0.1%)	4.50 (0.1%)	4.50 (0.1%)
5	28.95	29.47	29.47	29.49	29.49	29.4 (−0.3%)	29.38 (−0.3%)	29.48 (0.0%)	29.49 (0.0%)
8	74.38	76.79	76.87	76.86	76.94	76.7 (−0.1%)	76.76 (−0.1%)	76.8 (−0.1%)	76.93 (0.0%)

Table 6 Comparison of the density ratio for a nonreactive pure oxygen gas

M	NC [4, 5]	Theory				DSMC			
		HO [6]	HOe	aHO	aHOe	HO	HOe	aHO	aHOe
Scenario I									
2	2.68	2.68	2.68	2.68	2.68	2.68 (0.1%)	2.68 (0.1%)	2.68 (0.1%)	2.68 (0.1%)
5	5.05	5.05	5.05	5.05	5.05	5.05 (0.0%)	5.05 (0.0%)	5.05 (0.0%)	5.05 (0.0%)
8	5.62	5.73	5.73	5.74	5.74	5.72 (−0.0%)	5.73 (0.0%)	5.74 (−0.0%)	5.74 (−0.0%)
Scenario II									
2	2.68	2.68	2.68	2.68	2.68	2.67 (−0.3%)	2.67 (−0.3%)	2.67 (−0.3%)	2.67 (−0.3%)
5	5.05	5.11	5.11	5.11	5.11	5.11 (0.1%)	5.10 (−0.1%)	5.17 (1.1%)	5.12 (0.1%)
8	5.62	6.17	6.17	6.19	6.19	6.18 (0.2%)	6.17 (0.0%)	6.21 (0.3%)	6.21 (0.3%)
Scenario III									
2	2.68	2.68	2.68	2.68	2.68	2.67 (−0.3%)	2.67 (−0.3%)	2.67 (−0.3%)	2.67 (−0.3%)
5	5.05	5.46	5.46	5.47	5.48	5.48 (0.4%)	5.48 (0.4%)	5.47 (−0.1%)	5.48 (0.1%)
8	5.62	6.63	6.67	6.67	6.71	6.66 (0.5%)	6.70 (0.5%)	6.67 (0.0%)	6.71 (0.0%)

Table 7 Comparison of the temperature ratio for a nonreactive pure oxygen gas

M	NC [4, 5]	Theory				DSMC			
		HO [6]	HOe	aHO	aHOe	HO	HOe	aHO	aHOe
Scenario I									
2	1.68	1.68	1.68	1.68	1.68	1.68 (0.3%)	1.68 (0.3%)	1.68 (0.3%)	1.68 (0.3%)
5	5.74	5.74	5.74	5.74	5.74	5.73 (−0.1%)	5.73 (−0.1%)	5.73 (−0.1%)	5.73 (−0.1%)
8	13.23	13.04	13.04	13.02	13.02	13.06 (0.1%)	13.07 (0.2%)	13.05 (0.2%)	13.01 (−0.1%)
Scenario II									
2	1.68	1.68	1.68	1.68	1.68	1.69 (0.7%)	1.69 (0.7%)	1.69 (0.7%)	1.69 (0.7%)
5	5.74	5.69	5.69	5.68	5.68	5.66 (−0.5%)	5.67 (−0.3%)	5.69 (0.2%)	5.66 (−0.4%)
8	13.23	12.28	12.28	12.25	12.25	12.34 (0.5%)	12.25 (−0.3%)	12.25 (0.0%)	12.3 (0.4%)
Scenario III									
2	1.68	1.68	1.68	1.68	1.68	1.68 (0.1%)	1.68 (0.1%)	1.68 (0.1%)	1.68 (0.1%)
5	5.74	5.4	5.4	5.39	5.39	5.36 (−0.8%)	5.36 (−0.8%)	5.39 (0.0%)	5.39 (0.0%)
8	13.23	11.58	11.52	11.53	11.47	11.53 (−0.5%)	11.46 (−0.6%)	11.52 (−0.1%)	11.47 (0.0%)

of electronic energies is correctly recovered by the DSMC simulations. As the upstream Mach number increases, there is a slight increase in the equilibrium pressure as more of the physics is accounted for (either by including the electronic energy or by switching from HO to aHO). Similar observations are found for scenarios II and III with the difference that the departure from ideal gas theory occurs at lower Mach numbers. The pressure ratio is found to be insensitive to the vibrational model and the inclusion of the electronic mode. However, in scenario III, the pressure ratio is underestimated by almost 3.5% if the caloric imperfection is neglected.

The study follows with the evaluation of the gas density equilibrium state reached behind the shock. Table 6 repeats the previous comparison with the density ratio. Analogously to the pressure ratio, the density ratio deviates from the standard normal shock wave relations at the same Mach number. This behaviour is expected as the downstream temperatures are too low to promote the electronic mode that starts to significantly impact the solution for any temperature above 1500 K [33], see Table 3. Table 6 shows that for scenario I, the density ratio calculated from the newly derived Rankine–Hugoniot jump relations is in excellent agreement with those calculated with Eggers' [6] corrections. For scenario II and a high Mach number, the downstream temperatures are high enough to activate the electronic mode; therefore, a slight increase is noticeable in the downstream density when the electronic mode is added. For scenario III, the density ratio appreciably deviates from ideal gas theory and the corrected Rankine–Hugoniot relations depart from Eggers' [6] corrections for any Mach number above 3. Considering the aHOe solution to be the most physically realistic, the ideal gas theory under-predicts the density ratio by 19% at Mach 8, and Eggers' solution under-predicts the density ratio by 1.2%.

Table 7 presents the temperature ratios. The Rankine–Hugoniot calculations and DSMC simulations are found to be in excellent agreement. Like the pressure and density ratios, the post-shock equilibrium temperature ratios perfectly agree with ideal gas theory up to Mach number 6.8 for scenario I, Mach number 4.4 for scenario II, and Mach number 2.6 for scenario III. Again, this is anticipated by the thermal states reached after the shock which promote the vibrational and electronic modes. As mentioned in the above section, there is an increase in density ratio with the addition of the electronic mode, whereas, the pressure profile remains relatively unchanged from the increase of the upstream Mach number. To maintain the thermal equation of state, the thermal state has to balance at a lower temperature than when the electronic mode is neglected from the internal modes. Considering scenario III, the ideal gas theory under-estimates the temperature ratio, compared to the aHOe solution, by a factor of 13%, which corresponds to a difference of about 350 K downstream of the shock wave. Similarly, the decrease of about 13% in the temperature ratio coincides with an increase of 3.5% in the pressure ratio and an increase of 19% in the density ratio. The aHOe temperature ratio for scenario III at Mach 8 is 1.2% lower than Eggers' solution. Table 7 demonstrates that the thermal equation of state is well maintained, having a lower thermal equilibrium state after the shock with the electronic mode included.

Furthermore, an analysis of the departure from ideality is also conducted by comparing the Rankine–Hugoniot jump relations and the DSMC results. Figures 3, 4, and 5 present a comparison of the theoretical and numerical macroscopic flow property ratios across a normal shock against ideal gas theory for scenarios I, II, and III, respectively. The flow property ratios are normalised by their corresponding ideal gas theory flow properties ratios, e.g., $\rho_{21}^{\mathrm{HO}}/\rho_{21}^{*}$. Such a nor-

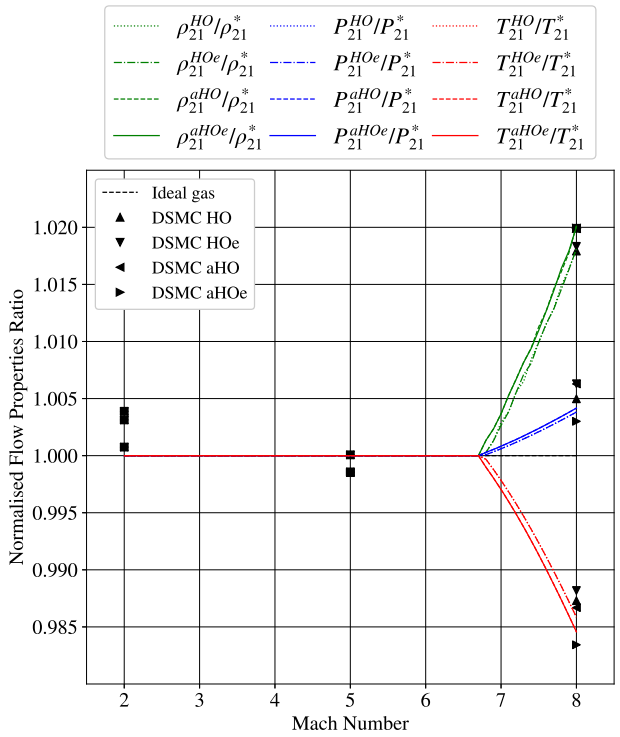

Fig. 3 Flow properties ratio of a pure oxygen gas exhibiting caloric imperfection for scenario I

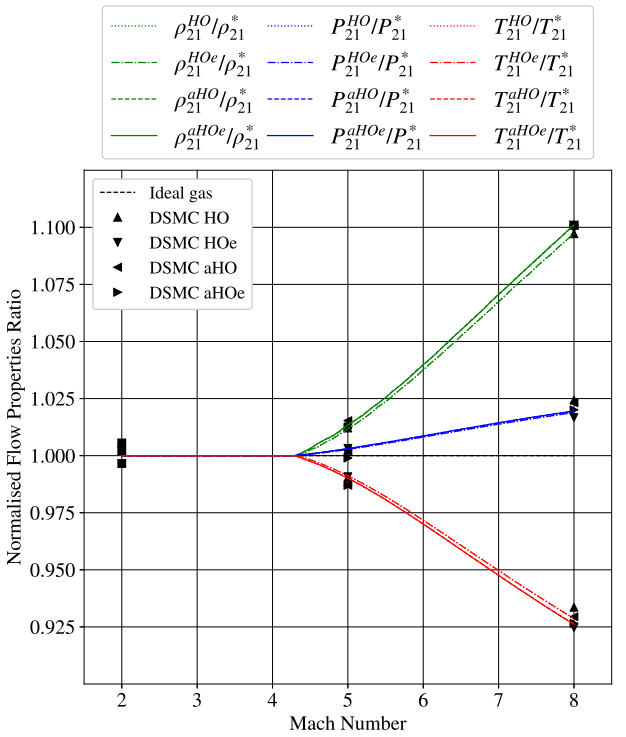

Fig. 4 Flow properties ratio of a pure oxygen gas exhibiting caloric imperfection for scenario II

malisation allows the ideality theory to be represented by a straight line, drawn with a black dashed line along 1.000 on the ordinate axis. The normalised density, temperature, and pressure profiles are plotted with green, red, and blue lines, respectively.

In Fig. 3, the numerical results present discrepancies with the theoretical predictions for the pressure and temperature ratios for scenario I. The ordinate axis has been scaled such that it closes up on the plotted graphs, hence, magnifying the differences between the numerical and theoretical results. Additionally, the difference is merely the percentage deviation presented in Tables 5, 6, and 7. Furthermore, in scenario I ($h_1 = 3.14 \times 10^5$ J/kg), the downstream enthalpy for Mach numbers 2, 5, and 8 is, with the most sophisticated correction, i.e., aHOe, 3.14×10^5 J/kg, 3.14×10^5 J/kg, and 4.20×10^5 J/kg. The downstream enthalpies only differ from the freestream enthalpy for Mach number 8, to the extent that deviations from ideal gas theory are nearly negligible, thereby magnifying the disparities between the numerical and theoretical results.

In Figs. 3, 4, and 5, the gas is only considered calorically imperfect, therefore the thermal equation of state stands. If the density of the gas increases across the shock, the temperature must undergo a proportional decrease. This effect has previously been illustrated in Tables 5, 6, and 7, and it is reiterated in Figs. 3 and 4. The numerical results recover the Rankine–Hugoniot relations well, suggesting a strong

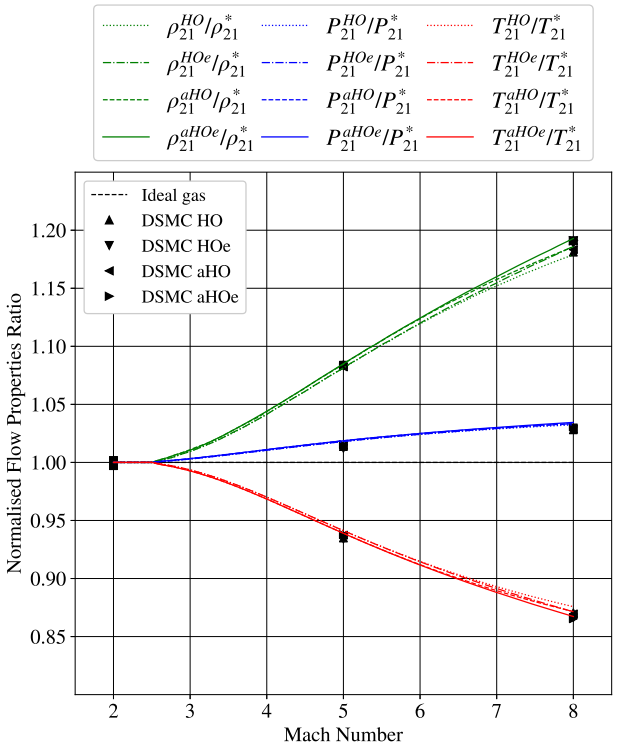

Fig. 5 Flow properties ratio of a pure oxygen gas exhibiting caloric imperfection for scenario III

Table 8 Comparison of the pressure ratio for a nonreactive gas mixture, composed of 79% nitrogen and 21% oxygen

M	NC [4, 5]	Theory				DSMC			
		HO [6]	HOe	aHO	aHOe	HO	HOe	aHO	aHOe
Scenario I									
2	4.50	4.50	4.50	4.50	4.50	4.50 (−0.0%)	4.50 (−0.0%)	4.50 (−0.0%)	4.50 (−0.0%)
5	28.97	28.97	28.97	28.97	28.97	28.91 (−0.2%)	28.91 (−0.2%)	28.91 (−0.2%)	28.91 (−0.2%)
8	74.41	74.49	74.49	74.51	74.51	74.6 (0.1%)	74.58 (0.1%)	74.23 (−0.4%)	74.49 (−0.0%)
Scenario II									
2	4.5	4.5	4.5	4.5	4.5	4.51 (0.3%)	4.51 (0.3%)	4.51 (0.3%)	4.51 (0.3%)
5	28.97	28.98	28.98	28.98	28.98	29.05 (0.2%)	29.13 (0.5%)	29.0 (0.1%)	29.04 (0.2%)
8	74.41	75.41	75.41	75.45	75.45	75.32 (−0.1%)	75.5 (0.1%)	75.59 (0.2%)	75.23 (−0.3%)
Scenario III									
2	4.50	4.50	4.50	4.50	4.50	4.50 (0.1%)	4.50 (0.1%)	4.50 (0.1%)	4.50 (0.1%)
5	28.97	29.31	29.31	29.32	29.33	29.29 (−0.1%)	29.28 (−0.1%)	29.32 (0.0%)	29.32 (0.0%)
8	74.41	76.5	76.52	76.55	76.57	76.41 (−0.1%)	76.48 (0.0%)	76.52 (0.0%)	76.6 (0.0%)

departure from the ideality of the temperature and the density ratios for any Mach number above 6.8, 4.4, and 2.6 for scenarios I, II, and III, respectively. Figures 3, 4, and 5 suggest that modelling the vibrational energies with an aHO model and adding the electronic mode results in a greater deviation from ideal gas theory. At low upstream temperatures, i.e., scenario I, such as those found in wind-tunnels, the inclusion of electronic energy and an anharmonic oscillator model do not change the results compared to the models proposed by Eggers [6]; however, as the upstream temperature is increased towards those that would be found in typical flight conditions, i.e., scenario III, there is a clear deviation in the results when including electronic energy and modelling the vibrational energy with an aHO model. The result is that downstream of the shock, there will be a greater density and a lower temperature than that predicted by Eggers' model.

The inclusion of the electronic modes and modelling the vibrational excitation with an anharmonic oscillator model significantly increases the specific heat capacity, (3), and consequently the static enthalpy of the flow, (7), i.e., $\forall T, C_v^{\mathrm{aHO}}(T) > C_v^{\mathrm{HO}}(T)$). Note that the static enthalpy of the flow is governed by the upstream conditions; therefore, for a given static enthalpy, the HO model must predict a greater temperature. In addition, for the thermal equation of state to be maintained, a variation in the density ratio must be accompanied by a change in both pressure and temperature. As shown in Figs. 3, 4, and 5, the pressure exhibits a small deviation with the change of vibrational models. From (8), the density ratio varies as the inverse square root of the difference of enthalpy $\Delta\hat{h}_{21}$, which consequently imposes the density ratio to be lower with the HO model than it is for the aHOe model.

Note that a change in the upstream temperature, T_1, drastically influences the distribution of the internal energy in the system. Such a physical insight is observable when comparing the departure from ideal gas theory and Eggers' correction in Figs. 3, 4, and 5. An increase of T_1 leads to an increase of the populations of the high-lying vibrational quantum levels and the electronic excited states, resulting in a strong departure from ideal gas theory and Eggers' correction at a lower Mach number. Conversely, a decrease in T_1 will have the opposite influence where only the first few vibrational quantum levels will be populated resulting in the caloric imperfection being negligible.

4.3 Air mixture shock wave

In this section, flow properties across a normal shock wave are studied for a nonreactive gas mixture composed of 79% nitrogen and 21% oxygen. Like the previous section, the vibrational models are denoted by their corresponding acronyms and the inclusion of the electronic mode by HOe or aHOe. The standard normal shock wave relations [4, 5] without the consideration of caloric imperfection are denoted by NC.

The comparison of the pressure ratio is presented in Table 8. It is found that the Rankine–Hugoniot relations are in very good agreement with the numerical results. Similar to the oxygen test case, the caloric imperfection of the gas has a limited impact on the pressure across the normal shock wave. The four corrections predict a similar difference to the standard normal shock relations regardless of the upstream temperature. Overall, the choice of the vibrational model and the inclusion of electronic energies have an insignificant influence on the pressure ratio.

The gas mixture study follows with the comparison of the density ratio tabulated in Table 9. Note that a change in the flow density has a considerable impact on the other thermo-

Table 9 Comparison of the density ratio for a nonreactive gas mixture, composed of 79% nitrogen and 21% oxygen

M	NC [4, 5]	Theory				DSMC			
		HO [6]	HOe	aHO	aHOe	HO	HOe	aHO	aHOe
Scenario I									
2	2.67	2.67	2.67	2.67	2.67	2.68 (0.1%)	2.68 (0.1%)	2.68 (0.1%)	2.68 (0.1%)
5	5.03	5.03	5.03	5.03	5.03	5.03 (−0.0%)	5.03 (−0.0%)	5.03 (−0.0%)	5.03 (−0.0%)
8	5.61	5.64	5.64	5.64	5.64	5.64 (0.0%)	5.64 (0.0%)	5.64 (−0.0%)	5.64 (−0.0%)
Scenario II									
2	2.67	2.67	2.67	2.67	2.67	2.68 (0.3%)	2.68 (0.3%)	2.68 (0.3%)	2.68 (0.3%)
5	5.03	5.04	5.04	5.05	5.05	5.05 (0.0%)	5.05 (0.1%)	5.05 (0.1%)	5.05 (−0.0%)
8	5.61	5.99	5.99	6.0	6.0	5.99 (0.1%)	5.98 (−0.0%)	6.0 (−0.0%)	6.0 (0.0%)
Scenario III									
2	2.67	2.67	2.67	2.67	2.67	2.67 (−0.2%)	2.67 (−0.2%)	2.67 (−0.2%)	2.67 (−0.2%)
5	5.03	5.30	5.30	5.31	5.31	5.30 (0.0%)	5.30 (0.0%)	5.31 (0.0%)	5.31 (0.0%)
8	5.61	6.45	6.46	6.48	6.49	6.46 (0.1%)	6.47 (0.1%)	6.48 (0.0%)	6.49 (0.0%)

dynamic properties of the system. It is therefore important to correctly capture this flow property. In Table 9, the Rankine–Hugoniot relations are found to be in excellent agreement with the numerical results. It is also interesting to notice that for the same upstream temperature, the electronic mode only becomes excited at a higher Mach number. Such behaviour is a result of the composition of the gaseous mixture considered, in which the main component is molecular nitrogen. The caloric imperfection shown by the oxygen molecule at low temperature, see Sect. 4.2, is therefore hidden by the influence of the nitrogen molecule delaying the appearance of the electronic mode influence to higher flow temperatures. Similar to the oxygen test case, it is clear that the density ratio across the shock wave is not considerably impacted until very high Mach numbers and high freestream temperatures. For scenario I, the density ratio undergoes a significant change from ideal gas theory for a Mach number of 7.5, whereas for scenario II it appreciably deviates at Mach number 4.9, and at Mach number 3.0 for scenario III. The addition of the electronic mode of the molecule leads to a small increase in the density ratio behind the shock at high Mach numbers and higher upstream thermal states.

Since the temperature is linearly related to the pressure and inversely proportional to the density due to the thermal equation of state, the results in Table 10 can be regarded as a consequence of the two above discussions; the temperature should balance at a lower thermal state when the flow density downstream of the shock increases. According to Tables 8, 9, and 10, this is the case with a quasi-constant pressure, an increase of the flow density, and a decrease in similar proportions for the downstream temperature. It is important to note that the thermal equation of state is perfectly conserved and that the flow properties returned by the DSMC simulations match the predictions of the mathematical description of the caloric imperfection laid out in Sect. 2. As pointed out in the density ratio, the Rankine–Hugoniot relations deviate from ideal gas theory at a Mach number of 7.5, 4.9, and 3.0 for scenarios I, II, and III, respectively. The caloric imperfection is therefore appreciable for Mach numbers above these limitations with a maximum deviation in the temperature ratio of 1% (3 K), 5% (69 K), and 11% (292 K) for scenarios I, II, and III, respectively. Additionally, the newly derived Rankine–Hugoniot relations suggest lower temperature ratios compared to those predicted with Eggers' correction.

Figures 6, 7, and 8 compare the DSMC simulation results to the mathematical modelling of the caloric imperfection of the gas, and the correction suggested in Eggers' work [6]. The flow property ratios are normalised as in the previous section on a pure oxygen gas. The Rankine–Hugoniot predictions are drawn with lines whose colours depend on the flow property being considered. The ideal gas theory is included for reference and is represented with a black dashed line along 1.000 on the ordinate axis.

Figure 6 indicates a misalignment between the DSMC results and the theoretical predictions, although Table 8 shows a small percentage deviation. Similar conclusions to those obtained for the pure oxygen gas in scenario, see Fig. 3, can here be drawn with the difference of the freestream enthalpy which is $h_1 = 3.49 \times 10^5$ J/kg and the downstream enthalpies which are 3.49×10^5 J/kg, 3.49×10^5 J/kg, and 4.66×10^5 J/kg for Mach numbers 2, 5, and 8, respectively.

It is evident that for scenarios II and III there is excellent agreement between the caloric imperfection modelling, the DSMC simulations, and Eggers' correction [6]. Eggers studied the imperfection of an air mixture with the HO model and electronic energy being disabled. From Figs. 6, 7, and 8, it is important to notice that the present work constitutes an exten-

Table 10 Comparison of the temperature ratio for a nonreactive gas mixture, composed of 79% nitrogen and 21% oxygen

M	NC [4, 5]	Theory				DSMC			
		HO [6]	HOe	aHO	aHOe	HO	HOe	aHO	aHOe
Scenario I									
2	1.68	1.68	1.68	1.68	1.68	1.68 (−0.1%)	1.68 (−0.1%)	1.68 (−0.1%)	1.68 (−0.1%)
5	5.75	5.75	5.75	5.75	5.75	5.74 (−0.2%)	5.74 (−0.2%)	5.74 (−0.2%)	5.74 (−0.2%)
8	13.27	13.21	13.21	13.2	13.2	13.23 (0.1%)	13.22 (0.1%)	13.16 (−0.4%)	13.2 (−0.0%)
Scenario II									
2	1.68	1.68	1.68	1.68	1.68	1.68 (0.0%)	1.68 (0.0%)	1.68 (0.0%)	1.68 (0.0%)
5	5.75	5.75	5.75	5.74	5.74	5.76 (0.2%)	5.77 (0.4%)	5.74 (−0.1%)	5.75 (0.2%)
8	13.27	12.6	12.6	12.58	12.58	12.58 (−0.2%)	12.62 (0.2%)	12.6 (0.2%)	12.54 (−0.3%)
Scenario III									
2	1.68	1.68	1.68	1.68	1.68	1.69 (0.5%)	1.69 (0.5%)	1.69 (0.5%)	1.69 (0.5%)
5	5.75	5.53	5.53	5.52	5.52	5.52 (−0.2%)	5.52 (−0.2%)	5.52 (−0.1%)	5.52 (−0.1%)
8	13.27	11.85	11.84	11.81	11.80	11.83 (−0.2%)	11.82 (−0.2%)	11.81 (0.0%)	11.8 (0.0%)

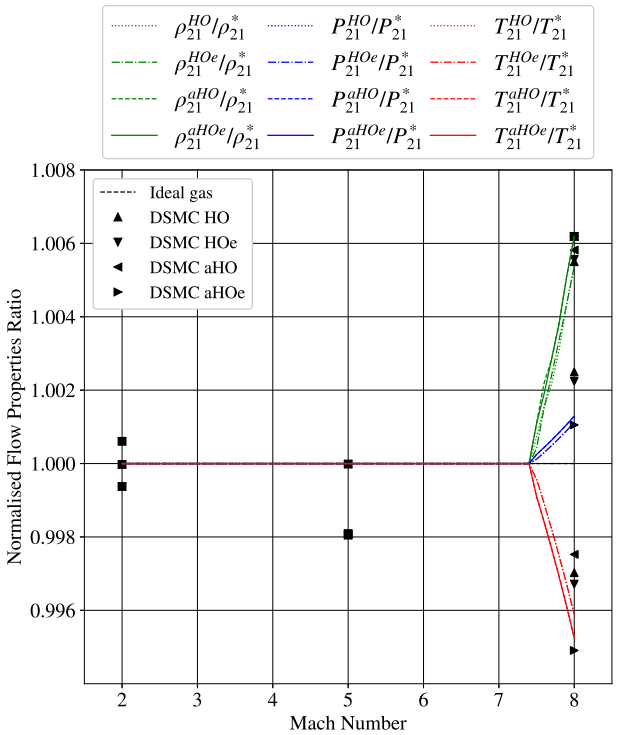

Fig. 6 Flow properties ratio of a gas mixture, composed of 79% nitrogen and 21% oxygen, exhibiting caloric imperfection for scenario I

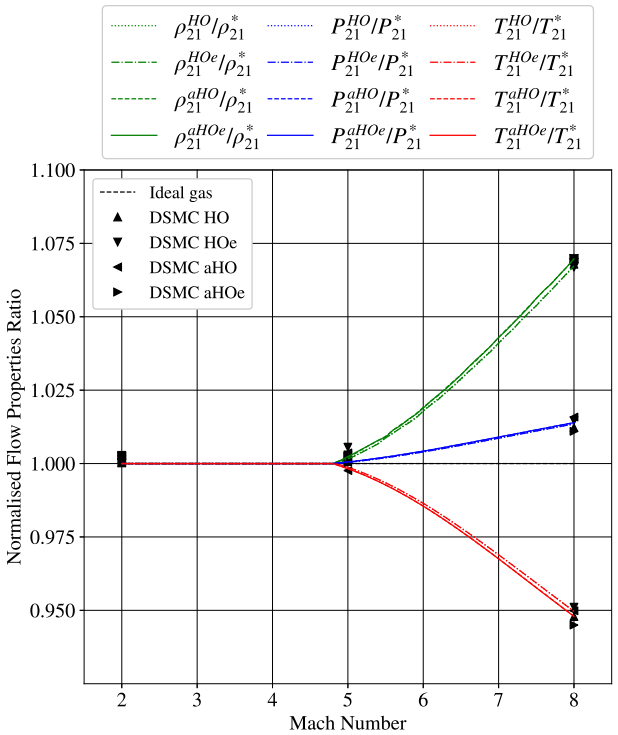

Fig. 7 Flow properties ratio of a gas mixture, composed of 79% nitrogen and 21% oxygen, exhibiting caloric imperfection for scenario II

sion to the work achieved by Eggers with the modelling of the caloric imperfection, the inclusion of electronic energies of the molecule, and by addressing the vibrational excitation with an aHO model.

The findings in the above sections can also be observed in Figs. 6, 7, and 8. For the two wind-tunnel operating conditions, i.e., scenarios I and II, the aHO model and the inclusion of the electronic mode have no significant contributions to the downstream flow properties; however, for scenario III, which is more representative of real flight conditions, the aHO model and the inclusion of the electronic mode begin to contribute and the flow properties deviating not only from ideal gas theory but also from one another. The study suggests that the inclusion of the electronic mode and the modelling

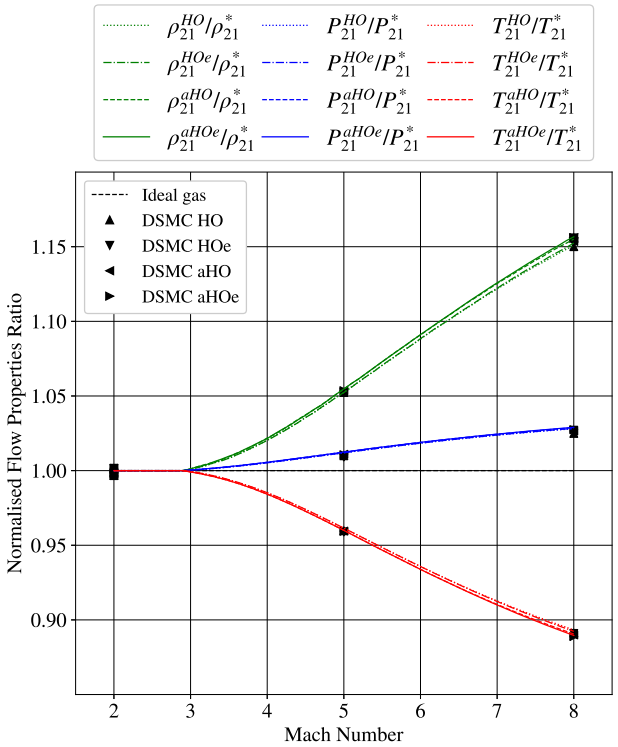

Fig. 8 Flow properties ratio of a gas mixture, composed of 79% nitrogen and 21% oxygen, exhibiting caloric imperfection for scenario III

with an aHO model enhance the deviation from ideality. These two contributions have proven to better match the specific heat capacity suggested by McBride et al. [24] laid out in Sect. 4.1. Therefore, this would likely imply that the real gas effects are closer to the aHOe notation referred to in Figs. 6, 7, and 8, highlighting an under-estimation in the flow density of 20% if the ideal gas theory is considered and 1.2% different to Eggers' predictions. Modelling vibrational excitation with an aHO model and including the electronic mode constitutes a significant improvement; however, some work has to be done in the direction of coupling rotational-vibrational-electronic effects at high temperature to better model the physics of the flow.

5 Conclusions

The Rankine–Hugoniot jump relations for calorically imperfect gases are extended to include the vibrational excitation being modelled with an aHO model and to include the electronic mode of the molecule. The merits of these considerations are quantified and discussed for shock waves at two wind-tunnel operating conditions (scenarios I and II) and one more realistic flight condition (scenario III). The Rankine–Hugoniot relations outline good physical insights of the caloric imperfections for both wind-tunnel conditions and flight conditions.

The calculations show an excellent agreement with DSMC simulations for a range of Mach numbers between 2 and 8. The gas exhibits a strong departure from ideality for any Mach number above 6.8, 4.4, and 2.6 for a pure oxygen gas in scenarios I, II, and III, respectively, and for any Mach number above 7.5, 4.9, and 3.0 for an air mixture in scenarios I, II, and III, respectively. The importance of including the electronic mode for reproducing the correct thermophysical properties is illustrated; it amplifies the departure from ideality. In scenario III, the traditional HO model and the Morse-aHO model diverge above Mach number 3.0 for pure oxygen gas and Mach number 5.0 for the air mixture; as a result, the use of the HO model is questionable for all but relatively low enthalpy flow. In addition, the air mixture calculations suggest that the temperature ratios exhibit a significant deviation of up to 11% at Mach 8 from ideality and the density ratio reveals a strong deviation of up to 16% at Mach 8 from ideality. The pressure ratio is not impacted as severely, with a maximum departure up to 3% reached at Mach 8.

In the present work, the coupling between the internal modes of the molecular systems has been disregarded. In future work, the coupling between the vibrational and electronic mode and its influence on the flow properties will be addressed. Further studies on the influence of modelling the vibrational excitation with an aHO model will be presented. The next step in terms of quantifying the influence of such a change is the extension to chemically reactive gas flows.

References

1. Swantek, A., Austin, J.M.: Heat transfer on a double wedge geometry in hypervelocity air and nitrogen flows. 50th AIAA Aerospace Sciences Meeting Including the New Horizons Forum and Aerospace Exposition, Nashville, TN, AIAA Paper 2012-0284 (2012). https://doi.org/10.2514/6.2012-284
2. Knisely, A.M., Austin, J.M.: Geometry and test-time effects on hypervelocity shock-boundary layer interaction. 54th AIAA

Aerospace Sciences Meeting, San Diego, CA, AIAA Paper 2016-1979 (2016). https://doi.org/10.2514/6.2016-1979
3. Ninni, D., Bonelli, F., Colonna, G., Pascazio, G.: Unsteady behavior and thermochemical non equilibrium effects in hypersonic double-wedge flows. Acta Astronaut. **191**, 178–192 (2022). https://doi.org/10.1016/j.actaastro.2021.10.040
4. Rankine, W.J.M.: XV. On the thermodynamic theory of waves of finite longitudinal disturbance. Philos. Trans. R. Soc. Lond. **160**, 277–288 (1870)
5. Hugoniot, H.: Mémoire sur la propagation du mouvement dans un fluide indéfini (seconde partie). Journal de Mathématiques Pures et Appliquées **4**, 153–168 (1888)
6. Eggers, A.J.: One-dimensional flows of an imperfect diatomic gas. Technical Report TR-959, National Advisory Committee for Aeronautics (1949). https://ntrs.nasa.gov/citations/19930090933
7. Bethe, H.A., Teller, E.: Deviations from thermal equilibrium in shock waves. Technical Report NP-4898; BRL-X-117, Aberdeen, Ballistics Research Laboratory, MD (1953). https://www.osti.gov/servlets/purl/4420349
8. NASA Ames Research Staff: Charts for compressible flow. Technical Report TR-1135, National Aeronautics and Space Administration Ames Aeronautical Laboratory (1953). https://ntrs.nasa.gov/citations/19930091059
9. Blackman, V.: Vibrational relaxation in oxygen and nitrogen. J. Fluid Mech. **1**(1), 61–85 (1956). https://doi.org/10.1017/S0022112056000056
10. Ibraguimova, L.B., Sergievskaya, A.L., Levashov, V.Y., Shatalov, O.P., Tunik, Y.V., Zabelinsk, I.E., II.: Investigation of oxygen dissociation and vibrational relaxation at temperatures 4000–10800 K. J. Chem. Phys. **139**(3), 034317 (2013). https://doi.org/10.1063/1.4813070
11. Streicher, J.W., Krish, A., Hanson, R.K., Hanquist, K.M., Chaudhry, R.S., Boyd, I.D.: Shock-tube measurements of coupled vibration–dissociation time-histories and rate parameters in oxygen and argon mixtures from 5000 K to 10000 K. Phys. Fluids **32**(7), 076103 (2020). https://doi.org/10.1063/5.0012426
12. Bird, G.A.: Aspects of the structure of strong shock waves. Phys. Fluids **13**(5), 1172–1177 (1970). https://doi.org/10.1063/1.1693047
13. Bird, G.A.: Molecular Gas Dynamics and the Direct Simulation of Gas Flows. Oxford University Press, New York (1994)
14. Elizarova, T.G., Khokhlov, A.A., Montero, S.: Numerical simulation of shock wave structure in nitrogen. Phys. Fluids **19**(6), 068102 (2007). https://doi.org/10.1063/1.2738606
15. Timokhin, M.Y., Struchtrup, H., Kokhanchik, A.A., Bondar, Y.A.: Different variants of R13 moment equations applied to the shock-wave structure. Phys. Fluids **29**(3), 037105 (2017). https://doi.org/10.1063/1.4977978
16. Todorova, B.N., White, C., Steijl, R.: Numerical evaluation of novel kinetic models for binary gas mixture flows. Phys. Fluids **32**(1), 016102 (2020). https://doi.org/10.1063/1.5134040
17. Alsmeyer, H.: Density profiles in argon and nitrogen shock waves measured by the absorption of an electron beam. J. Fluid Mech. **74**(3), 497–513 (1976). https://doi.org/10.1017/S0022112076001912
18. Greenshields, C.J., Reese, J.M.: The structure of shock waves as a test of Brenner's modifications to the Navier–Stokes equations. J. Fluid Mech. **580**, 407–429 (2007). https://doi.org/10.1017/S0022112007005575
19. Goodwin, D.G., Moffat, H.K., Speth, R.L.: Cantera: an object-oriented software toolkit for chemical kinetics, thermodynamics, and transport processes, version 2.5.1 (2018). https://doi.org/10.5281/zenodo.4527812
20. McBride, B.J., Gordon, S., Reno, M.A.: Thermodynamic data for fifty reference elements. Technical Report TP-3287, National Aeronautics and Space Administration (2001). https://ntrs.nasa.gov/citations/20010021116
21. Gordon, S., McBride, B.J.: Computer program for calculation of complex chemical equilibrium compositions and applications. Part 1: Analysis. Technical Report RP-1311, National Aeronautics and Space Administration (1994). https://ntrs.nasa.gov/citations/19950013764
22. McBride, B.J., Gordon, S.: Computer program for calculation of complex chemical equilibrium compositions and applications. Part 2: Users manual and program description. Technical Report RP-1311, National Aeronautics and Space Administration (1996). https://ntrs.nasa.gov/citations/19960044559
23. McBride, B.J., Gordon, S., Reno, M.A.: Coefficients for calculating thermodynamic and transport properties of individual species. Technical Report TM-4513, National Aeronautics and Space Administration (1993). https://ntrs.nasa.gov/citations/19940013151
24. McBride, B.J., Zehe, J., M., Gordon, S.: NASA Glenn coefficients for calculating thermodynamic properties of individual species. Technical Report TP-2002-211556, National Aeronautics and Space Administration (2002). https://ntrs.nasa.gov/citations/20020085330
25. Martín, M.P.: Direct numerical simulation of hypersonic turbulent boundary layers. Part 1: initialization and comparison with experiments. J. Fluid Mech. **570**, 347–364 (2007). https://doi.org/10.1017/S0022112006003107
26. Passiatore, D., Sciacovelli, L., Cinnella, P., Pascazio, G.: Thermochemical non-equilibrium effects in turbulent hypersonic boundary layers. J. Fluid Mech. **941**, A21 (2022). https://doi.org/10.1017/jfm.2022.283
27. Schouler, M., Prévereaud, Y., Mieussens, L.: IXV post-flight reconstruction and analysis of the aerothermodynamic measurements along the rarefied portion of the reentry trajectory. Int. J. Heat Mass Transf. **178**, 121582 (2021). https://doi.org/10.1016/j.ijheatmasstransfer.2021.121582
28. Liepmann, H.W., Roshko, A.: Elements of Gas Dynamics. Wiley, Hoboken (1957)
29. Zhu, T., Li, Z., Levin, D.A.: Modeling of unsteady shock tube flows using direct simulation Monte Carlo. J. Thermophys. Heat Transf. **28**(4), 623–634 (2014). https://doi.org/10.2514/1.T4419
30. Lofthouse, A.J., Boyd, I.D., Wright, M.J.: Effects of continuum breakdown on hypersonic aerothermodynamics. Phys. Fluids **19**(2), 027105 (2007). https://doi.org/10.1063/1.2710289
31. Shoev, G., Vashchenkov, P., Shevyrin, A., Bondar, Y.: Validation of DSMC and NS computations for high-enthalpy non-equilibrium flows in ground and flight tests. AIP Conf. Proc. **2132**(1), 070007 (2019). https://doi.org/10.1063/1.5119561
32. Kustova, E., Alekseev, I., Tan, L.: Investigation of shock wave structure in CO_2 based on the continuum and DSMC approaches. J. Phys. Conf. Ser. **1959**(1), 012032 (2021). https://doi.org/10.1088/1742-6596/1959/1/012032
33. Civrais, C.H.B., White, C., Steijl, R.: Vibrational modeling with an anharmonic oscillator model in direct simulation Monte Carlo. J. Thermophys. Heat Transf. **37**(3), 534–548 (2022). https://doi.org/10.2514/1.T6547
34. Nompelis, I., Candler, G.: Investigation of hypersonic double-cone flow experiments at high enthalpy in the LENS facility. 45th AIAA Aerospace Sciences Meeting and Exhibit, Reno, NV, AIAA Paper 2007-203 (2007). https://doi.org/10.2514/6.2007-203
35. Khapra, D., Patel, A.: Shock wave structure in non-polar diatomic and poly-atomic dense gases under rotation and vibration. Phys. Fluids **34**(6), 066115 (2022). https://doi.org/10.1063/5.0097397
36. Roy, R.J.L.: LEVEL: a computer program for solving the radial Schrödinger equation for bound and quasibound levels. J. Quant. Spectrosc. Radiat. Transf. **186**, 167–178 (2017). https://doi.org/10.1016/j.jqsrt.2016.05.028

37. Morse, P.M.: Diatomic molecules according to the wave mechanics. II. Vibrational levels. Phys. Rev. **34**(1), 57 (1929). https://doi.org/10.1103/PhysRev.34.57
38. Capitelli, M., Colonna, G., Giordano, D., Maraffa, L., Casavola, A., Minelli, P., Pagano, D., Pietanza, L.D., Taccogna, F.: Tables of internal partition functions and thermodynamic properties of high–temperature mars-atmosphere species from 50 K to 50,000 K. Technical Report STR-246, European Space Agency Publications Division (2005)
39. Vincenti, W.G., Kruger, C.H.: Introduction to Physical Gas Dynamics. Wiley, New York (1965)
40. Castellan, G.W.: Physical Chemistry. Addison-Wesley, Boston (1983)
41. Liechty, D.S., Lewis, M.J.: Extension of the quantum-kinetic model to lunar and mars return physics. Phys. Fluids **26**(2), 027106 (2014). https://doi.org/10.1063/1.4866319
42. NIST: National Institute for Standards and Technology (NIST) Chemistry WebBook. https://kinetics.nist.gov/kinetics/index.jsp
43. Anderson, J.D.: Hypersonic and High-Temperature Gas Dynamics. American Institute of Aeronautics and Astronautics, Reston (2006)
44. National Oceanic and Atmospheric Administration: U.S. Standard Atmosphere. Technical Report TM-X-74335, National Aeronautics and Space Administration (1976). https://ntrs.nasa.gov/citations/19770009539
45. Leyva, I.A.: The relentless pursuit of hypersonic flight. Phys. Today **70**(11), 30–36 (2017). https://doi.org/10.1063/PT.3.3762
46. Civrais, C.H.B., White, C., Steijl, R.: Evaluation of a kinetic-theory approach for chemical-reaction rates in upper-atmosphere hypersonic flows. AIAA AVIATION 2023 Forum, San Diego, CA, AIAA Paper 2023-3809 (2023). https://doi.org/10.2514/6.2023-3809
47. Fowler, R.H., Guggenheim, E.A.: Statistical Thermodynamics. Cambridge University Press, New York (1939)
48. Beckwith, I.E., Miller, C.G., III.: Aerothermodynamics and transition in high-speed wind tunnels at NASA Langley. Annu. Rev. Fluid Mech. **22**(1), 419–439 (1990). https://doi.org/10.1146/annurev.fl.22.010190.002223
49. White, C., Borg, M.K., Scanlon, T.J., Longshaw, S., John, B., Emerson, D.R., Reese, J.M.: dsmcFoam+: an OpenFOAM based direct simulation Monte Carlo solver. Comput. Phys. Commun. **224**, 22–43 (2018). https://doi.org/10.1016/j.cpc.2017.09.030
50. Weller, H.C., Tabor, G., Jasak, H., Fureby, C.: A tensorial approach to computational continuum mechanics using object-oriented techniques. Comput. Phys. **12**(6), 620–631 (1998). https://doi.org/10.1063/1.168744
51. Civrais, C.H.B., White, C., Steijl, R.: Influence of an anharmonic oscillator model for flows over a cylindrical body. AIP Conf. Proc. **(accepted)** (2023)
52. Armenise, I., Esposito, F.: N_2, O_2, NO state-to-state vibrational kinetics in hypersonic boundary layers: the problem of rescaling rate coefficients to uniform vibrational ladders. Chem. Phys. **446**, 30–46 (2015). https://doi.org/10.1016/j.chemphys.2014.11.004
53. Bergemann, F., Boyd, I.D.: New Discrete Vibrational Energy Model for the Direct Simulation Monte Carlo Method, pp. 174–183. American Institute of Aeronautics and Astronautics (1994). https://doi.org/10.2514/5.9781600866302.0174.0183
54. Bird, G.A.: Perception of numerical methods in rarefied gasdynamics. Prog. Astronaut. Aeronaut. **117**, 211–226 (1989). https://doi.org/10.2514/5.9781600865923.0211.0226
55. Bird, G.A.: Definition of mean free path for real gases. Phys. Fluids **26**(11), 3222–3223 (1983). https://doi.org/10.1063/1.864095
56. Wysong, I.J., Gimelshein, S.F., Bondar, Y., Ivanov, M.: Comparison of direct simulation Monte Carlo chemistry and vibrational models applied to oxygen shock measurements. Phys. Fluids **26**(4), 043101 (2014). https://doi.org/10.1063/1.4871023
57. McBride, B.J., Gordon, S.: Computer program for calculating and fitting thermodynamic functions. Technical Report RP-1271, National Aeronautics and Space Administration (1992). https://ntrs.nasa.gov/citations/19930003779